SUPPORTING INFORMATION

CO$_2$ electroreduction to formate at a partial current density of 930 mA cm^{-2} with InP colloidal quantum dot derived catalysts

*Ivan Grigioni,[†, ‡, |] Laxmi Kishore Sagar,[†, |] Yuguang C. Li,[†] Geonhui Lee,[†] Yu Yan,[†] Koen Bertens,[†] Rui Kai Miao,[§] Xue Wang,[†] Jehad Abed,[†] Da Hye Won,[†,||] F. Pelayo García de Arquer,[†] Alexander H. Ip,[†] David Sinton,[§] Edward H. Sargent[†, *]*

[†] Department of Electrical and Computer Engineering, University of Toronto, 35 St. George St., Toronto, Ontario M5S 1A4, Canada.

[‡] Dipartimento di Chimica, Università degli Studi di Milano, Via Golgi 19, 20133 Milano, Italy

[||] Clean Energy Research Center, Korea Institute of Science and Technology, Seoul 02792, Republic of Korea

[§] Department of Mechanical and Industrial Engineering, University of Toronto, 5 King's College Rd., Toronto, Ontario M5S 3G8, Canada.

[|] These authors contributed equally

[*] Corresponding author

Supporting Information

1   Experimental section

2   Supporting experimental data

1 Experimental section

1.1 Materials and chemicals

KOH, indium acetate (99.99%, In(OAc)$_3$), 1-octadecene (90%, ODE), oleic acid (90%), Tris(trimethylsilyl)-phosphine ((TMSi)$_3$P), Trioctylphosphine (97%, TOP), 6-mercapto-1-hexanol (MCH), dimethyl sulfoxide, deuterated water (D$_2$O), indium nitrate (99.9%, In(NO$_3$)$_3$) Nafion perfluorinated resin solution 5 wt. %, methanol, hexane, toluene and isopropyl alcohol (both HPLC grade) were used as purchased from Aldrich, TCI and other suppliers. CO$_2$ (99.99%) and Ar (99.999%) were purchased from Linde. Carbon cloth (CC) CeTech W1S1009, CeTech W1S1010 and Sigracet 35 BC were purchased from Fuel Cell store.

1.2 InP colloidal quantum dots (CQDs) synthesis

InP QDs were synthesized using a modified approach.[1] In a typical synthesis, 0.100 g (0.34 mmol) of In(OAc)$_3$, 0.282 g (1 mmol) of oleic acid and 8 mL of ODE were added to a 25 mL Schlenk flask. The reaction mixture was degassed under vacuum at 110˚C for 90 minutes. The flow was switched to nitrogen and the flask was cooled to room temperature. Inside a nitrogen-filled glovebox, phosphorous precursor solution was prepared in a 10 mL vial by adding 1 mL (0.23 mmol) of (TMSi)$_3$P-ODE solution and 1.5 mL TOP under continuous stirring. The (TMSi)$_3$P precursor solution was injected into the In(OAc)$_3$ solution at room temperature, and the reaction mixture was heated to 310˚C for 10 minutes to obtain InP QDs. QDs were purified 2 times using hexane/isopropanol and ethanol as solvent and anti-solvent combination. Purified dots were dispersed in hexane.

6-mercapto-1-hexanol ligand exchange process:[2] 25 mg of purified InP QDs dispersed in 3 mL hexane were taken in a test tube. MCH (1 mmol, 140 µL) was swiftly added and the resulting solution was vortexed vigorously for 15 minutes. InP QDs were precipitated by adding a 1 mL of toluene and centrifuged at 7500 rpm for 3 min. The supernatant was discarded

and the precipitate was dispersed in ethanol with sonication and filtered with a 0.22 µm PTFE syringe filter.

1.3 CQDs characterization: UV-Vis, XRPD, TEM, XPS and RAMAN spectroscopy

InP CQDs UV-Vis characterization was performed with a PerkinElmer Lambda900 spectrophotometer and the quantum dot concentration was evaluated by evaporating at 60°C a known amount of CQDs methanol solution and measuring the weight of the solid deposit.

XRPD Measurement. XRPD samples were prepared by drop-casting a layer of the desired material from hexane solution on a glass substrate. Measurements were performed on a Rigaku powder diffractometer.

TEM Measurement. All transmission electron microscopy (TEM) images were acquired on a Hitachi HF 3300 electron microscope operating at 300 keV. TEM samples were prepared by drop-casting a purified solution of CQDs from hexanes onto a 300-mesh copper grid with a carbon film (SPI supplies). ImageJ was employed to generate the size of the dots.

X-ray Photoelectron Spectroscopy (XPS). XPS spectra were measured using a Thermo Scientific K-Alpha system with an Al Kα source. The CQDs films were prepared on glass substrates by spin coating a CQDs solution at 2000 RPM. A 50 eV pass energy and scans were taken at 0.05 eV steps.

In situ Raman measurements were operated with a water immersion objective using a Renishaw inVia Raman microscope. The spectra were collected using 785 nm laser with 10-s-integration. An open-structured flow cell was utilized for the measurements. An Ag/AgCl electrode (filled with saturated aqueous KCl solution) and a platinum wire were used as the reference and counter electrode, respectively.

1.4   Electrode preparation

The electrodes were prepared by drop casting a solution obtained by adding 50, 100, 150 µL of the InP CQDs solution (with total amount of CQDs of 80, 160 and 240 µg) to 550, 500 or 450 µL of methanol, respectively, then 10 µL of Nafion solution was added. The solution was added dropwise to a 2x2 cm^2 carbon cloth piece heated at 50°C on a hotplate to facilitate evaporation. Once the solution was added completely the electrode was dried for 30 minutes at 50°C. The control electrodes were prepared with the same procedure: the CC was coated with Nafion and with the ligand containing solution which was prepared by adding 10 µL of Nafion or 10 µL of 6-mercapto-1-hexanol to 600 µL of methanol, respectively. The In_2O_3 control electrode was prepared by spray coating a precursor ink containing 40 mg of In_2O_3 100 nm nanoparticles dispersed by sonication for 1 hour in 4 mL of MeOH containing 40 µL of Nafion.

In_2O_3 controls were prepared by spray coating onto CC. We found that, in the case of drop casting, ink drops result in an uneven distribution of catalyst. In the spray-coating approach, we used a catalyst loading that allowed complete coverage of the CC, and we used an In_2O_3:Nafion ratio that allows CO_2 and H_2O availability at the catalyst surface.[3] In this way we established a study that was not dominated by CO_2 and H_2O availability; nor by the carbon cloth hydrogen evolution activity; but that instead allowed us to study and compare InP CQD based electrodes.

The use of CQDs capped with the native ligand resulted in a suboptimal dispersion of the CQDs or of the Nafion ionomer. Indeed, native CQDs can be easily dispersed in hexane, due to the high hydrophobicity of the ligands, however Nafion is immiscible in hexane and rapidly aggregates. This leads to an inhomogeneous precursor ink. On the other hand, by introducing CQDs capped with the native ligand in the MeOH solution containing the Nafion ionomer

results in agglomeration of the CQDs. Therefore, we sought to exchange the highly hydrophobic ligand with 6-mercaptohexanol (6-MPE) which is more hydrophilic and allowed us to obtain a stable and homogeneous ink.

Initially, different conductive substrate was investigated as possible GDL. PTFE based GDL: in the case of PTFE coated with brush sprayed conductive carbon (PTFE/C) or with sputtered copper (PTFE/Cu) the InP CQDs solution directly passes through the GDL. This is reasonably due to the mild hydrophobic nature of the 6-MPA ligand which probably allows the permeation of the CQDs through the hydrophobic PTFE microporous layer. Several carbon papers and carbon cloths has been also tested (all from Fuel Cell store). In this case the CQDs remain on the hydrophobic side of the conductive GDL but flooding occurred abruptly right after the electrolyte contacted the electrode.

Few substrates were able to maintain a good stability against flooding. The CeTech W1S1009, which was used in most experiments. However, its large pores make it prone to electrolyte infiltration in long term experiments or when pressure fluctuations occur. CeTech W1S1010 and Sigracet 35 BC was employed in the stability test since was found to be less affected by flooding.

1.5   <u>Electrochemical characterization</u>

The electrochemical characterization of the cathodes in the CO_2 reduction reaction was performed using a potentiostat (Autolab PGSTAT302N), a custom-made flow cell having a fixed 1x1 cm^2 electrode geometric area,[3] two peristaltic pumps connected to the flow cell with silicone tubing and a digital mass flow controller (Sierra, SmartTrack 100). For experiments at current higher than -400 mA a current booster (Metrohm Autolab, 10 A) was connected to the potentiostat. The electrolyte solutions were freshly prepared with milli-Q water. The small 2.4 nm dots were used in most of the experiments and a fresh electrode was employed for each

electrochemical test, unless otherwise stated in the text. A CO_2 flow of 50 mL min^{-1} was employed in all experiments.

Commercial nickel foam was used as anode and an Ag/AgCl 1 M KCl was used as reference electrode (see section 2.6 and ref. 3 for further details on flow cell assembly). The applied potential was converted to the reversible hydrogen electrode (RHE) by using the following equation (eq. 1):

$$E_{RHE} = E_{Ag/AgCl} + 0.059 * pH + E^{\circ}_{Ag/AgCl} \qquad \text{eq.1}$$

with $E^{\circ}_{Ag/AgCl}$ = 0.197 V and $E_{Ag/AgCl}$ is the applied potential with respect to the Ag/AgCl reference electrode.

1.6   Liquid and gas product analysis

Liquid products were analyzed with HPLC. A volume of 30 mL or 200 mL for stability tests was continuously recirculated inside the anode and the cathode compartments. For measures of liquid samples after 20 minutes of CO_2RR at -400 mA cm^{-2} 100 μL of anolyte and catholyte was directly injected in the HPLC. While for more concentrated solution, the analyte was diluted with pure electrolyte to obtain a final concentration within the employed calibration curve (50-0.05 10^{-3} mol L^{-1} of formate). The Faradaic efficiency to formate is calculated as sum of the formate collected in the cathode and anode sides.

For experiments at different current density, we collected the samples for liquid product analysis after 480 Coulombs was passed through the electrolyzer. We maintained constant this value (the charge passed in 20 minutes at a current of 400 mA) to have a consistent sampling time in each experiment.

Nuclear magnetic resonance (NMR) spectroscopy of catholyte solutions was used to evaluate the presence of other liquid products. The NMR sample was prepared inside the NMR tube by

7

mixing 100 µL of analyte (catholyte or anolyte), 100 µL of internal standard solution dimethyl sulfoxide (DMSO), and 400 µL of D_2O. ^{1}HNMR spectra were collected with an Agilent DD2 500 spectrometer in water suppression mode. The data were analyzed by using the MestReNova software.

Gas product analysis was carried out by sampling 1 mL of gas at the CO_2 outlet of the flow cell on the cathode side. A gastight Hamilton chromatographic syringe was employed and analysis was repeated at least two time for each specific sampling time (with a 200s time interval between each reproducibility analysis) The sampled gas was injected into a gas chromatograph (PerkinElmer Clarus 680), equipped with a thermal conductivity detector (TCD), flame ionization detector (FID), and packed columns (Molecular Sieve 5A and Carboxen-1000). Argon (Linde, 99.999%) was used as carrier gas in the gas chromatograph. The GC was periodically calibrated to attain the calibration values which allowed to calculate the amount of gas products contained in the sampled volume.

1.7   Cathodic energy efficiency calculation

The cathodic energy efficiency (CEE, half-cell efficiency) for formate was calculated at a certain applied potential with the following eq. 1

$$CEE_{formate} = \frac{FE_{formate} \; x \; E^0_{formate}}{E^0_{H_2O} - V} \qquad\qquad \text{eq. 1}$$

where $FE_{formate}$ is the faradaic efficiency to formate, $E^0_{formate}$ is the thermodynamic cell potential of formate formation (1.48 V_{RHE}),[4] $E^0_{H_2O}$ is the thermodynamic potential for water oxidation (1.23 V_{RHE}) at the anode and V is the applied potential; all potential are vs. RHE.[3]

2 Supporting experimental data

2.1 Control experiments
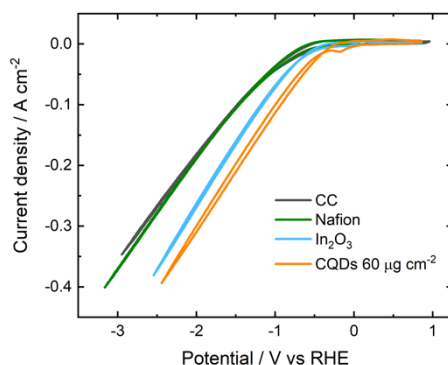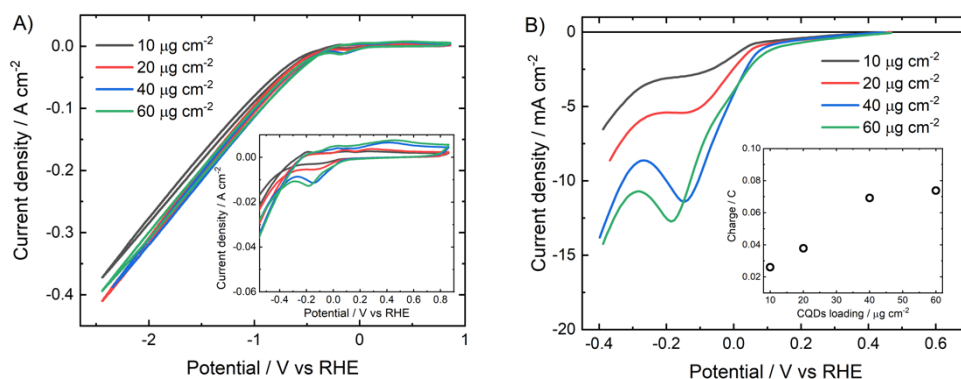

Figure S1. Cyclic voltammetry with CO_2 in a flow cell: in 1 M KOH for: unmodified carbon cloth (CC); CC coated with 10 uL of Nafion solution; CC coated with In_2O_3 nanoparticles with 100 nm diameter and CC coated with InP CQDs.

Figure S1 shows the cyclic voltammetry of the control electrodes. **Table S1** reports the faradaic efficiencies for H_2, CO, and formate recorded during chronoamperometry at -400 mA cm^{-2} with: (lines 1-5) control experiments and (line 6-7) CC/InP loaded with 60 µg cm^{-2} electrode, as comparison. Trace amounts of CH_4 (ca. 0.1%) were also detected with the CQDs based cathodes. In general, the control experiments produce mainly H_2, while a low amount of formate was observed with the CC/ligand, possibly due to the presence of a sulfur moieties. The CC/In_2O_3 electrode also produces formate with a FE of ca. 60% over 1 hour. A CC/InP electrode produced only H_2 when N_2 was flowed instead of CO_2 (line 7).

Table S1. Faradaic Efficiencies recorded with the control electrodes

	Cathode	KOH / mol L^{-1}	Sampling / min	Current density / mA cm^{-2}	Faradaic efficiency / %		
					H_2 FE	CO FE	HCOO$^-$
1	CC	1	60	- 400	95.5 ± 1.9	0.0	1.2
2	CC/Nafion	1	60	- 400	98.5 ± 5.0	0	1.4
3	CC/ligand	1	60	- 400	94.5 ± 5.4	0.3	4.6
4	CC/In_2O_3	1	20	- 400	32.6 ± 5.8	0.5 ± 0	64.6
5	CC/In_2O_3	1	60	- 400	46.4	0.5	55.5
6	CC/InP	1	20	- 400	0.4± 0.05	5.3 ± 0.3	86.6
7	CC/InP – N_2	1	60	- 400	96.9 ± 3.0	0	0

9

2.2   Experiments with different CQDs loadings

Figure S2. A) Cyclic voltammetry with CO_2 in a flow cell in 1 M KOH for CC/InP electrodes with different CQDs loadings, 2.4 nm size. B) reduction wave of the In^{3+}/In^0 redox peak and charge passed during the reduction (inset) for CC/InP electrodes with different loadings.

In order to determine the optimal CQDs loading, CC/InP samples were prepared by varying the CQDs loading in the range 10 - 60 µg cm^{-2}. Cyclic voltammetry measures, repeated on two sets of samples, showed that the current density increases by increasing the loading up to 40 µg cm^{-2}, for a larger amount the current is slightly lower. The In^{3+}/In^0 redox peaks located at ca. -0.2 to 0.5 V_{RHE} become more obvious by increasing the amount of CQDs (inset of **Figure S2A** and **Figure S2B**). However, the amount of charge passed during the reduction half cycle, calculated as the integral of the reduction current curve in **Figure S2B** multiplied by the reduction time, plateaus after a loading of 40 µg cm^{-2}. This suggests that the number of redox sites decreases per amount of CQDs reasonably due to coalescence and aggregation of the CQDs for loadings larger than 40 µg cm^{-2}.

The FEs recorded during chronoamperometries at different CQDs loadings are reported in **Table S2**. During the first 20 minutes of reaction, the FE for formate was ca. 90% for all loadings, with the electrode with 20 µg cm^{-2} loading outperforming the other three. The FE to CO slightly increases for larger loadings. For these reasons, we chose to carry out the further characterizations with a loading of 20 µg cm^{-2}. With this amount we achieved the highest FE to formate by minimizing CO production and the In content.

With this optimal loading we performed four 20-minutes long tests by employing each time a fresh cathode (lines 3 and 9-11 of Table S2), achieving an average FE to formate of 91.8 ± 1.0%.

Table S2. FE recorded with electrodes containing different CQDs loadings in 1M KOH.

	Cathode	Loading / µg cm^{-2}	Sampling / min	Current density / mA cm^{-2}	Faradaic efficiency / %		
					H$_2$ FE	CO FE	HCOO$^-$
1	CC/InP	10	20	- 400	0.4 ± 0.1	4.8 ± 0.3	86.6
2	CC/InP	10	60	- 400	-	-	70.8
3	CC/InP	20	20	- 400	2.7 ± 0	5.2 ± 0.3	92.1
4	CC/InP	20	60	- 400	4.6± 0.2	4.7 ± 0.2	84.1
5	CC/InP	40	20	- 400	0.6	10.8	88.1
6	CC/InP	40	60	- 400	-	-	53.8
7	CC/InP	60	20	- 400	0.6 ± 0.2	9.3 ± 1.5	89.7
8	CC/InP	60	60	- 400	-	-	76.2
9	CC/InP	20	20	- 400	3.8 ± 0.4	4.9 ± 0.5	93.0
10	CC/InP	20	20	- 400	0.5 ± 0.1	5.5 ± 0.4	92.3
11	CC/InP	20	20	- 400	1.9 ± 0.8	5.3 ± 0.3	89.7
12	Average of the value in lines 3, 9-11				2.2 ± 1.0	5.2 ± 0.2	91.8 ± 1.0

For each loading we also extended the chronoamperometry tests up to 1 hour (**Table S2**), in all cases the FE to formate was found to decrease. This is likely due to flooding, leading to a more severe hydrogen evolution reaction, in line with data discussed in the main text. However, flooding was found to occur without any trend related to the loading amount, and further experiments suggest that other effects, such as pressure of the catholyte over the CC GDL, play more important roles in determining the stability of the overall electrochemical performances. See also **Section 2.5** for a detailed description of the stability tests.

2.3 Effect of KOH concentration and faradaic efficiencies at different current densities
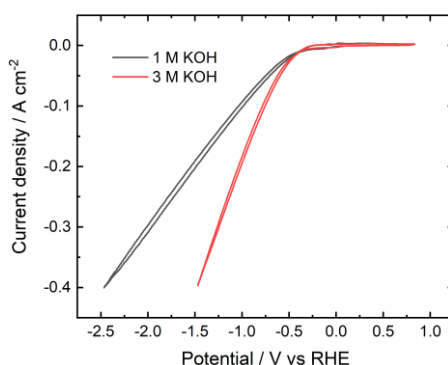
Figure S3. A) Cyclic voltammetry in CO_2RR in a flow cell with 1 M and 3 M KOH for CC/InP electrodes containing 20 µg cm^{-2} of CQDs.

Table S3 reports the FE at -0.4, -0.6, -0.8 and -1.0 A cm^{-2} discussed in the main text.

Line 5 of **Table S3** reports the FE recorded at -1.5 A cm^{-2}. The FE to formate was 90.3% leading to a current to formate of 1.35 A cm^{-2}. However, the potential was unstable reasonably due to the extreme reaction condition. During the reaction at -1.0 and -1.5 A cm^{-2} the electrolyte temperature increased from room temperature to ca. 40°C.

Table S3. Faradaic Efficiencies recorded at different applied current density in the flow cell, 3 M KOH and with an electrode containing 20 µg cm^{-2} of CQDs.

	Cathode	KOH / mol L^{-1}	Sampling / min	Current density / mA cm^{-2}	Faradaic efficiency / %		
					H_2 FE	CO FE	HCOO-
1	CC/InP	3	20	- 400	1.1 ± 0.5	5.3 ± 0.3	93.7
2	CC/InP	3	13.3	- 600	0.9 ± 0.6	6.7 ± 0.8	93.3
3	CC/InP	3	10	- 800	5.6 ± 1.1	6.4 ± 0.9	91.1
4	CC/InP	3	8	- 1000	0.5 ± 0.2	8.4 ± 0.3	93.1
5	CC/InP	3	5.3	- 1500	3.4	9.2	90.3

2.4 NMR representative spectrum
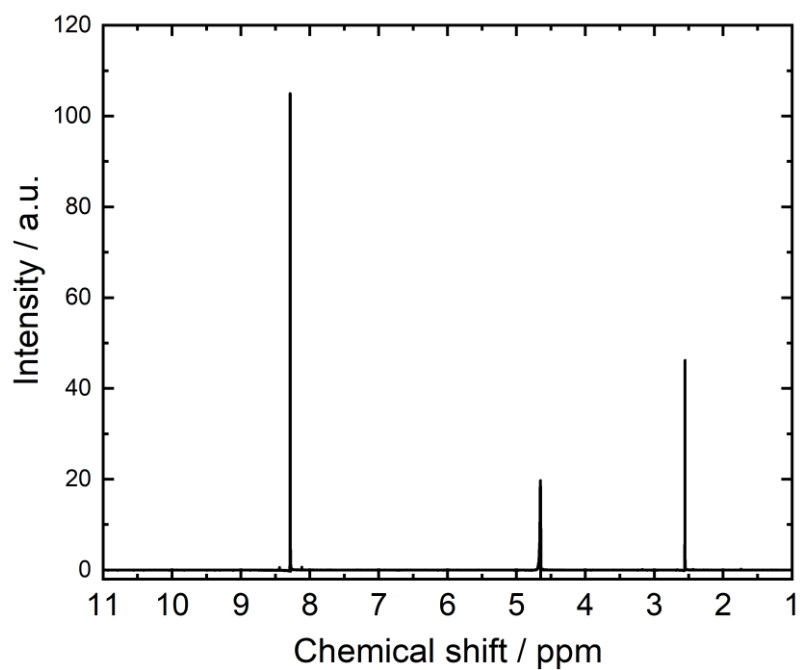
Figure S4. Representative nuclear magnetic resonance (NMR) spectrum of the catholyte; peak of DMSO internal standard is at 2.5 ppm, formate peak at 8.3 ppm, the peak at 4.7 ppm is the residual of water signal after suppression.

2.5   Preliminary stability test and optimization of the CC substrate.
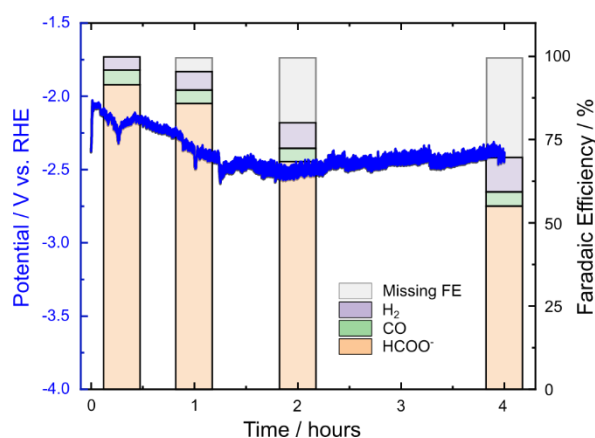
Figure S5. 4-hour chronopotentiometry at -400 mA cm^{-2} (blue trace and left Y axis) and Faradaic efficiencies at different sampling times (right Y axis) recorded with the CC/InP electrode loaded with 20 µg cm-2 of CQDs with 30 mL of 1 M KOH electrolytes.

We initially tested the stability of the InP CQDs by using the CeTech W1S1009 carbon cloth and a catholyte volume of 30 mL. During a 4 hour-long test, the formate FE (FE_{HCOO^-}) was ca. 90% in the first hour (**Figure S4** and **Table SI4**) with an impressive formate current density (J_{HCOO^-}) of 360 mA cm^{-2}. CO FE and H$_2$ FE are around 4% and 5% respectively. After one hour the formate concentration in the 30 mL catholyte reached ca. 0.20 mol L^{-1} with a formation rate of 5.9 mmol h^{-1} cm^{-2}.

However, after 2 and 4 hours of continuous operation, the FE_{HCOO^-} decreases to 70% and 61%, respectively. GDL flooding and formate crossover account for this decrease. Indeed, though the employed CC conductive GDL exhibited the best stability among the substrates initially tested (**see Section 1.4**), its progressive flooding led to a shortage of CO$_2$ at the catalyst/electrolyte interface and to the increase of HER over CO$_2$RR (see **Table S4**). The total FE, calculated as the sum of the FE for formate (in the anolyte and catholyte), H$_2$ and CO, was only of 82% and 76% after 2 and 4 hours, respectively. The missing FE is reasonably due to the partial oxidation of formate crossed from the cathode compartment through the anion exchange membrane to the anode side, where it is oxidized. Crossover increases as formate gets more concentrated in the catholyte.

14

Table S4. Faradaic Efficiencies recorded during the 4 hour-long test in the flow cell, 30 mL of 1 M KOH as catholyte and anolyte and with an electrode containing 20 µg cm^{-2} of CQDs.

|	Cathode	KOH / mol L^{-1}	Sampling / min	Current density / mA cm^{-2}	Faradaic efficiency / %		
					H$_2$ FE	CO FE	HCOO$^-$
1	CC/InP	1	20	- 400	3.8 ± 0.4	4.9 ± 0.5	93.0
2	CC/InP	1	60	- 400	5.6 ± 0.5	4.2 ± 0.4	87.4
3	CC/InP	1	120	- 400	8.0 ± 0.2	4.0 ± 0.3	70.2
4	CC/InP	1	240	- 400	10.7 ± 0.2	4.3 ± 0.8	60.2

To limit crossover, we used larger volumes of electrolytes, 200 mL instead of 30 mL. CeTech W1S1010 and Sigracet 35 BC carbon cloths showed better results, partially preventing flooding. Therefore for the stability test in **Figure 2c** we employed 200 mL of catholyte and anolyte and Sigracet 35 BC. Formate production was stable during a 4 hour long test with FE_{HCOO^-} higher than 90%.

We also performed stability tests in 3M KOH. However, we observed flooding not related to catalyst after two hours of continuous operation leading to a sudden shift from CO$_2$RR to HER.

Table S5. Faradaic Efficiencies recorded during the 4 hour-long test in the flow cell, with 200 mL of 1 M KOH as catholyte and anolyte and with an electrode containing 20 µg cm^{-2} of CQDs deposited on Sigracet 35 BC carbon cloth.

	Cathode	KOH / mol L^{-1}	Sampling / min	Current density / mA cm^{-2}	Faradaic efficiency / %		
					H$_2$ FE	CO FE	HCOO$^-$
1	CC/InP	1	60	- 400	1.7 ± 0.6	5.1 ± 0.4	88.3
2	CC/InP	1	120	- 400	1.2 ± 0.2	5.5 ± 0.8	97.8
3	CC/InP	1	240	- 400	1.4	5.4	94.1

2.6   Regular and modified flow cell design
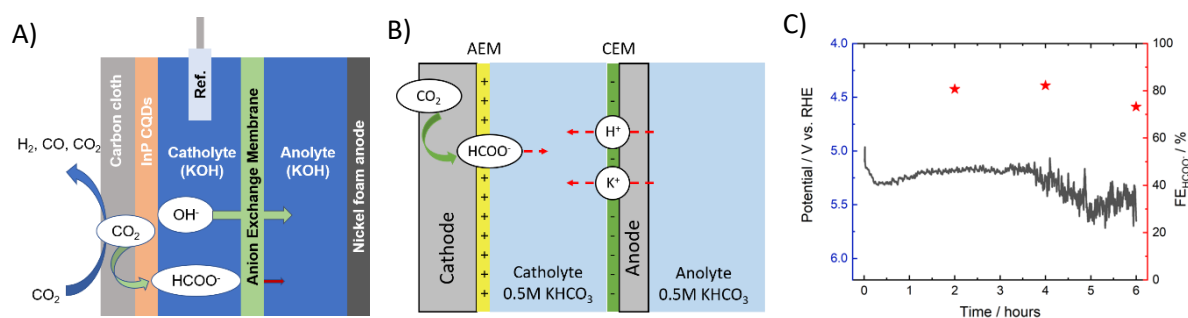
Figure S6. A) scheme of the regular flow cell, and B) scheme of the modified flow cell. C) Chronopotentiometry at -200 mA cm^{-2} recorded with a CC/InP electrode and 0.5 M KHCO$_3$ as electrolyte.

Figure S6A reports the regular flow cell architecture which we used in all experiments herein except where otherwise noted. The anode and the cathode are separated by an anion exchange membrane and the distance between the two electrodes is 2 cm. Aqueous KOH is used as catholyte and anolyte and the Ag/AgCl reference electrode is placed in the catholyte compartment. The electrolyzer is airtight, and two peristaltic pumps are used to flow the electrolytes in the two compartments. The gas diffusion electrode (carbon cloth coated with InP CQDs, left side) allows contact between the electrolyte and the CO$_2$ stream (the CO$_2$ flow is controlled with a mass flow controller, Sierra Instrument, C100L-DD-3-OV1). At the electrode/electrolyte junction, CO$_2$ reduction to formate (to H$_2$ and CO as gas products) occurs. Water acts as source of protons and the generated hydroxyl ions (OH$^-$) cross the anion exchange membrane and get oxidized at the anode (commercial nickel foam) generating oxygen. However, also formate, due to its negative charge, can cross the anion exchange membrane (this undesired process is indicated with a red arrow in **Figure S6A**) and can oxidize at the anode.

In order to overcome the instability caused by formate crossover and catholyte flooding, we modified the flow cell by inserting: i) an AEM between the GDE and the catholyte compartment (**Figure S6B**). ii) a cation exchange membrane (CEM) to separate the catholyte

16

and anolyte compartments and eliminate the crossover of negative charged formate into the anolyte, which may be oxidize back to CO_2.

The modified flow cell maintained a stable voltage of ~-5.2V (at -200mA cm^{-2}) for the first 4 hours with a stable FE_{HCOO^-} of ca. 80% (**Figure S6C**). However, the voltage starts fluctuating after 4 hours and the formate FE decreases to 73% after 6 hours. This is likely due to the precipitation of electrolyte salts in the catalyst layer. The high voltage is due to the use of an additional membrane and of neutral electrolyte (0.5 M $KHCO_3$), employed here to partially prevent salt formation, which is more severe in alkaline electrolyte.[5] The pH neutral condition also led to higher H_2 FE with respect to KOH electrolytes.

Table S6. Faradaic Efficiencies recorded with the modified flow cell (Mod. Flow-Cell, line 3-5).

|	Cathode	Cell type	Sampling / min	Current density / mA cm^{-2}	Faradaic efficiency / %		
					H$_2$ FE	CO FE	HCOO$^-$
1	CC/InP	Mod. Flow-Cell	120	- 200	12.1	7.9	80.7
2	CC/InP	Mod. Flow-Cell	240	- 200	13.5	5.8	82.2
3	CC/InP	Mod. Flow-Cell	360	- 200	24.4	1.6	73.3

2.7 Comparison with literature results

Table S7. Comparison with most relevant literature results for formic acid and formate production from CO_2RR

Electrolyte	Operating system	Applied Potential / V_{RHE}	J_{HCOO^-} / mA cm^{-2}	J_{HCOO^-} / mmol h^{-1} cm^{-2}	FE / %	Ref.	Year
3 M KOH	Flow cell	**-1.3 V_{RHE}**	**375**	**7.0**	**93.7**	**This work**	
3 M KOH	Flow cell	**-1.68 V_{RHE}**	**560**	**10.4**	**93.3**	**This work**	
3 M KOH	Flow cell	**-2.3 V_{RHE}**	**729**	**13.6**	**91.1**	**This work**	
3 M KOH	Flow cell	**-2.6 V_{RHE}**	**931**	**17.4**	**93.1**	**This work**	
0.5 M KHCO$_3$ 1 M KOH	Flow cell	-0.85 V_{RHE} -0.58 V_{RHE}	136 210	2.5	95 98	[6]	2019
2 M KHCO$_3$	Flow cell	-0.85 V_{RHE}	180	3.9	90	[7]	2018
Catholyte: 0.45 M KHCO$_3$ 0.5 M KCl Anolyte: 1 M KOH	Flow cell	-1.5 V_{RHE}	105	3.4	70	[8]	2017
1 M KHCO$_3$	Flow cell	-1.21 V_{RHE}	92.8	2.0	64	[9]	2018
0.1 M KHCO$_3$	Three electrode cell	-0.75 V_{RHE}	51.1	1.7	93	[10]	2017
0.1 M KHCO$_3$	H-cell	-0.85 V_{RHE}	67.5	1.0	90	[11]	2019
0.5 M CsHCO$_3$	H-cell	-0.98 V_{RHE}	78	1.3	93	[12]	2019
0.5 M KHCO$_3$	H-cell	-0.96 V_{RHE}	26.7	1.5	83	[13]	2017
0.5 M KHCO$_3$	H-cell	-1.16 V_{RHE}	57	0.5	95	[14]	2018
0.5 M KHCO$_3$	H-cell	-0.87 V_{RHE}	40	1.1	90	[15]	2020
Solid state electrolyte		-0.65 V_{RHE}	164	0.7	90	[16]	2019
Catholyte: 1 M KOH Anolyte: 0.4 M K$_2$SO$_4$	Flow cell with bipolar membrane	$E_{cell} = 5.9$ V	450	3.1	90	[17]	2020
0.1 M KHCO$_3$ H$_2$ oxidation as anodic reaction	Flow cell	-	375	8.4	75	[18]	2016
0.5 M Na$_2$SO$_4$ + 0.5 M Na$_2$CO$_3$ H$_2$ oxidation as anodic reaction	Flow cell	-0.94 V_{RHE}	277	7.0	72	[19]	2019

The performances reported in the last two rows of **Table S7** are obtained in flow cells running with hydrogen oxidation as anodic reaction,[18,19] due to the largely different experimental

condition these results were not reported in **Figure 2d** of the main text. Our highest J_{HCOO^-} is

2.5 and 3.4 times the of 375 and 277 mA cm^{-2} reported in these works.
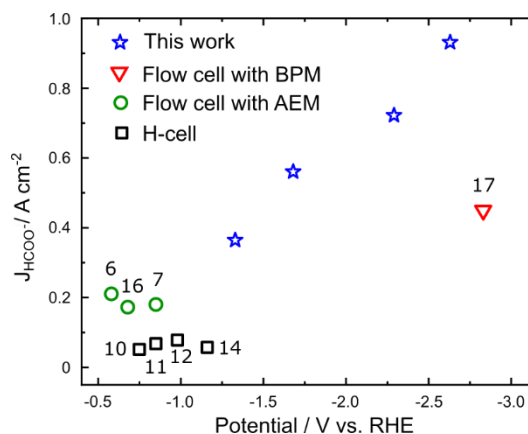
Figure S7. Comparison of current density for formate in 3 M KOH (open blue stars) relative to selected formate current density reported in the recent literature for H-cells (open black squares), flow cells with anion exchange membrane and solid state electrolyte (open green circle) and a flow cell with bipolar membrane (the potential is estimated from the cell potential reported by the authors). References are indicated in the Figure.

Figure S7 shows **Figure 2d** of the main text with the reference embedded in the figure.

2.8 In^{3+}/In^0 redox peaks: cyclovoltammetry at progressively larger cathodic potential
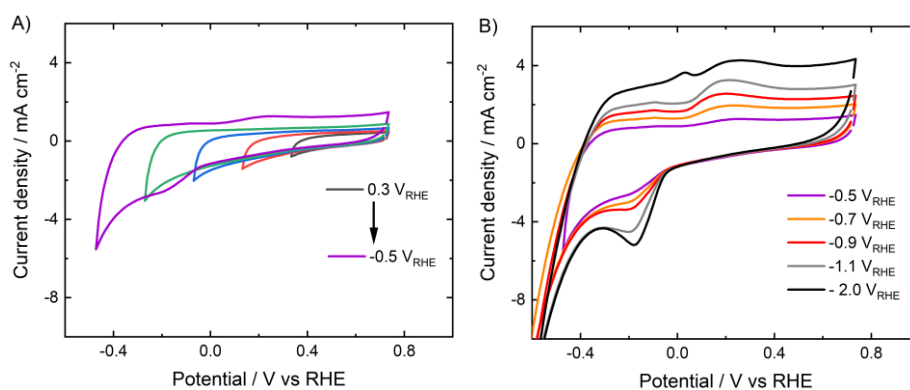
Figure S8. Cyclovoltammetry by progressively extending the cathodic half cycle deeper into negative potential from 0.8 to A) -0.5 and B) -2.0 V_{RHE}. The experiments were carried out in CO_2RR condition using a CC/InP electrode loaded with 20 µg cm^{-2} of CQDs, a scan rate of 50 mV s^{-1}, with each scan started from ca. 0.8 V_{RHE} (the open circuit potential of the electrode at the start of the experiment) and the potential was swept in the cathodic direction.

To assess if the redox peaks in the CQDs based cathode are already present before CO_2RR or if develop during CO_2RR, we carried out cyclovoltammetry by progressively extending the cathodic half cycle deeper into negative potential. **Figure S8A** shows that the redox feature appearing at potential below -0.5 V_{RHE} and becomes more obvious by applying more negative potentials (**Figure S8B**).

We carried out the cyclovoltammetry by sweeping the potential in the cathodic direction. No reduction peck (at ca. -0.2 V_{RHE} with negative current) was detected in the first half cycle. However, during the anodic half cycle, an oxidation peak at + 0.2-0.3 V_{RHE} appeared and in the following cathodic sweep the reduction peak at ca -0.2 V_{RHE} appeared. We infer that, during the first cathodic half cycle, at large reductive potential (see back trace in **Figure S8B**) surface In^{3+} (i.e. indium bonded with phosphorous as phosphide) is reduced to indium metal with phosphorous leaving the CQDs surface (confirmed by XPS). In the anodic direction In metal sites are oxidized back to In^{3+} and reduced again during the following cathodic half cycle.

In conclusion, In^{3+} is in situ reduced to indium metal which acts as catalytic site for CO_2 reduction.

2.9   Raman spectroscopy measures
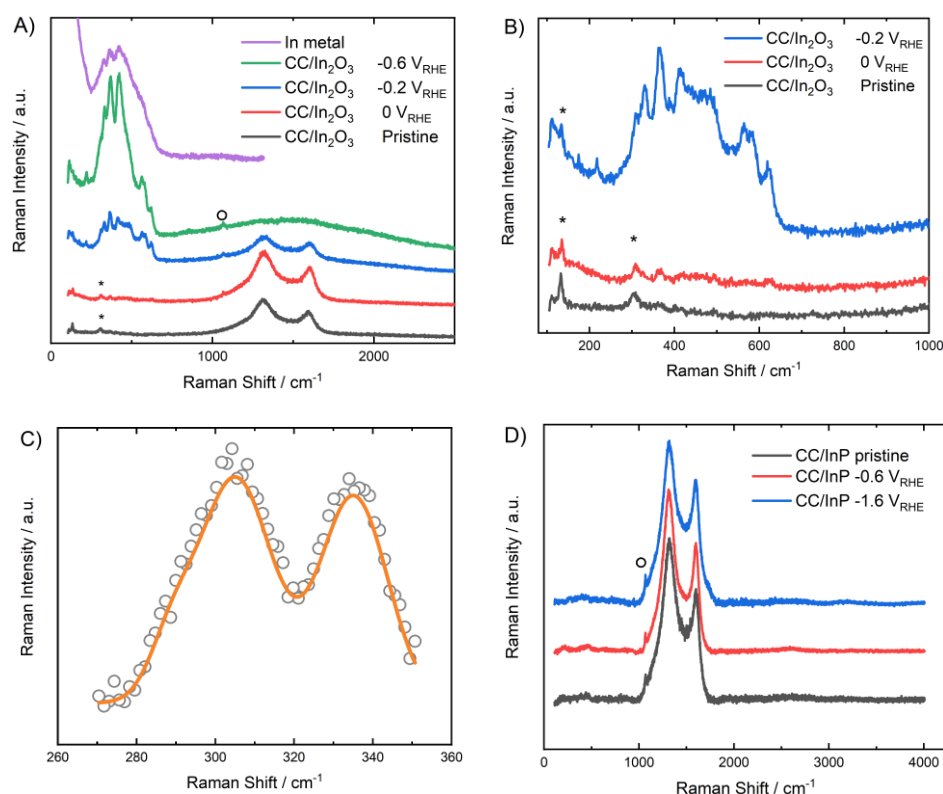
Figure S9. A) Operando Raman spectra of a CC/In_2O_3 electrode immersed in 1 M KOH in the presence of CO_2. The signature peak of In_2O_3 (indicated with a star) decreased at 0 V_{RHE} and progressively disappeared. The purple trace is In metal 100 mesh particles deposited on Si B) Same traces reported in **Figure S9A** showing a four times magnification of the frequency range relevant to the In_2O_3 signals (indicated with stars). C) Raman signal of InP CQDs deposited on Pt. D) CC/InP electrode containing 60 µg cm^{-2} of InP CQDs without an applied bias (black trace) and under CO_2RR condition in 1 M KOH and in the presence of CO_2; the signals is base corrected and normalized to the maximum to allow the comparison; the open circle indicates the carbonate signal.

In situ Raman spectroscopy was used to gain information on the electrode changes during CO_2RR and to observe surface adsorbed reaction intermediates.

Figure S9A shows the changes on a CC/In_2O_3 electrode, confirming that the pristine oxide (with signature peak at 135 and 307 cm^{-1}, **Figure S9B** show a magnification of the traces reported in **Figure S9A** to allow a better visualization of the potential-induced changes) is reduced under negative potential to In metal.[20] At -0.2 V_{RHE} In_2O_3 reduction already occurs and becomes more obvious at -0.6 V_{RHE}. The signal of metal indium is assigned by measuring the Raman spectrum of In particles 100 mesh on silicon (purple, top trace), which shows the

same fingerprint of reduced CC/In_2O_3 in the 250-700 cm^{-1}. This suggests that in CO_2RR experiments with CC/In_2O_3 (**Figure 2a, S1 and Table1**) the active catalyst is reduced In_2O_3 and this also confirms that the redox peak below 0 V_{RHE} shown in **Figure 2a, S2 and S8** for CC/InP is due to the reduction of In^{3+} to In^0. The doublet above 1000 cm^{-1} is typical of carbon and progressively disappears as indium metal is formed since it reflects the Raman IR laser.[21]

The Raman spectra of InP CQDs, **Figure S9C**, collected by depositing a concentrated drop of CQDs on platinum shows the InP doublet at 310 and 340 cm^{-1}.[22] However, the Raman spectra of CC/InP (obtained with a large loading of 60 $\mu g\ cm^{-2}$ of CQDs) **Figure S9D**, lack of the InP and In^0 signals. Even under a highly negative potential of -1.6 V_{RHE} any trace of In metal can be observed, reasonably due to the low amount of InP CQDs deposited on CC.

References

(1)   Ramasamy, P.; Ko, K. J.; Kang, J. W.; Lee, J. S. Two-Step "Seed-Mediated" Synthetic Approach to Colloidal Indium Phosphide Quantum Dots with High-Purity Photo- and Electroluminescence. *Chem. Mater.* **2018**, *30*, 3643–3647.

(2)   Wijaya, H.; Darwan, D.; Zhao, X.; Ong, E. W. Y.; Lim, K. R. G.; Wang, T.; Lim, L. J.; Khoo, K. H.; Tan, Z. K. Efficient Near-Infrared Light-Emitting Diodes Based on In(Zn)As–In(Zn)P–GaP–ZnS Quantum Dots. *Adv. Funct. Mater.* **2020**, *30*, 1–7.

(3)   García de Arquer, F. P.; Dinh, C.; Ozden, A.; Wicks, J.; Mccallum, C.; Kirmani, A. R.; Nam, D.; Gabardo, C.; Seifitokaldani, A.; Wang, X.; Li, Y. C.; Li, F.; Edwards, J. P.; Richter, L. J.; Thorpe, S. J.; Sinton, D.; Sargent, E. H. CO_2 Electrolysis to Multicarbon Products at Activities Greater than 1 A cm^{-2}. *Science.* **2020**, *367*, 661–666.

(4)   Verma, S.; Kim, B.; Jhong, H. R. M.; Ma, S.; Kenis, P. J. A. A Gross-Margin Model for Defining Technoeconomic Benchmarks in the Electroreduction of CO_2. *ChemSusChem* **2016**, *9*, 1972–1979.

(5)   Gabardo, C. M.; O'Brien, C. P.; Edwards, J. P.; McCallum, C.; Xu, Y.; Dinh, C. T.; Li, J.; Sargent, E. H.; Sinton, D. Continuous Carbon Dioxide Electroreduction to Concentrated Multi-Carbon Products Using a Membrane Electrode Assembly. *Joule* **2019**, *3*, 2777–2791.

(6)   Gong, Q.; Ding, P.; Xu, M.; Zhu, X.; Wang, M.; Deng, J.; Ma, Q.; Han, N.; Zhu, Y.; Lu, J.; Feng, Z.; Li, Y.; Zhou, W.; Li, Y. Structural Defects on Converted Bismuth Oxide Nanotubes Enable Highly Active Electrocatalysis of Carbon Dioxide Reduction. *Nat. Commun.* **2019**, *10*, 2807.

(7)   García de Arquer, F. P.; Bushuyev, O. S.; De Luna, P.; Dinh, C. T.; Seifitokaldani, A.; Saidaminov, M. I.; Tan, C. S.; Quan, L. N.; Proppe, A.; Kibria, M. G.; Kelley, S. O.; Sinton, D.; Sargent, E. H. 2D Metal Oxyhalide-Derived Catalysts for Efficient CO_2 Electroreduction. *Adv. Mater.* **2018**, *30*, 6–11.

(8)   Del Castillo, A.; Alvarez-Guerra, M.; Solla-Gullón, J.; Sáez, A.; Montiel, V.; Irabien, A. Sn Nanoparticles on Gas Diffusion Electrodes: Synthesis, Characterization and Use for Continuous CO_2 Electroreduction to Formate. *J. CO2 Util.* **2017**, *18*, 222–228.

(9)   Liang, C.; Kim, B.; Yang, S.; Yang Liu; Francisco Woellner, C.; Li, Z.; Vajtai, R.; Yang, W.; Wu, J.; Kenis, P. J. A.; Ajayan, P. M. High Efficiency Electrochemical Reduction of CO_2 beyond the Two-Electron Transfer Pathway on Grain Boundary Rich Ultra-Small SnO_2 Nanoparticles. *J. Mater. Chem. A* **2018**, *6*, 10313–10319.

(10)   Zheng, X.; De Luna, P.; García de Arquer, F. P.; Zhang, B.; Becknell, N.; Ross, M. B.; Li, Y.; Banis, M. N.; Li, Y.; Liu, M.; Voznyy, O.; Dinh, C. T.; Zhuang, T.; Stadler, P.; Cui, Y.; Du, X.; Yang, P.; Sargent, E. H. Sulfur-Modulated Tin Sites Enable Highly Selective Electrochemical Reduction of CO_2 to Formate. *Joule* **2017**, *1*, 794–805.

(11)   Luo, W.; Xie, W.; Li, M.; Zhang, J.; Züttel, A. 3D Hierarchical Porous Indium Catalyst for Highly Efficient Electroreduction of CO_2. *J. Mater. Chem. A* **2019**, *7*.

(12)   Ma, W.; Xie, S.; Zhang, X. G.; Sun, F.; Kang, J.; Jiang, Z.; Zhang, Q.; Wu, D. Y.; Wang, Y. Promoting Electrocatalytic CO_2 Reduction to Formate via Sulfur-Boosting Water

Activation on Indium Surfaces. *Nat. Commun.* **2019**, *10*, 892.

(13)   Chen, Z.; Yao, S.; Liu, L. 3D Hierarchical Porous Structured Carbon Nanotube Aerogel-Supported Sn Spheroidal Particles: An Efficient and Selective Catalyst for Electrochemical Reduction of CO_2 to Formate. *J. Mater. Chem. A* **2017**, *5*, 24651–24656.

(14)   He, S.; Ni, F.; Ji, Y.; Wang, L.; Wen, Y.; Bai, H.; Liu, G.; Zhang, Y.; Li, Y.; Zhang, B.; Peng, H.   The P-Orbital Delocalization of Main-Group Metals to Boost CO_2 Electroreduction . *Angew. Chemie* **2018**, *130*, 16346–16351.

(15)   Wu, D.; Huo, G.; Chen, W. Y.; Fu, X. Z.; Luo, J. L. Boosting Formate Production at High Current Density from CO_2 Electroreduction on Defect-Rich Hierarchical Mesoporous Bi/Bi_2O_3 Junction Nanosheets. *Appl. Catal. B Environ.* **2020**, *271*, 118957.

(16)   Xia, C.; Zhu, P.; Jiang, Q.; Pan, Y.; Liang, W.; Stavitsk, E.; Alshareef, H. N.; Wang, H. Continuous Production of Pure Liquid Fuel Solutions via Electrocatalytic CO_2 Reduction Using Solid-Electrolyte Devices. *Nat. Energy* **2019**, *4*, 776–785.

(17)   Chen, Y.; Vise, A.; Klein, W. E.; Cetinbas, F. C.; Myers, D. J.; Smith, W. A.; Deutsch, T. G.; Neyerlin, K. C. A Robust, Scalable Platform for the Electrochemical Conversion of CO_2 to Formate: Identifying Pathways to Higher Energy Efficiencies . *ACS Energy Lett.* **2020**, 1825–1833.

(18)   Kopljar, D.; Wagner, N.; Klemm, E. Transferring Electrochemical CO_2 Reduction from Semi-Batch into Continuous Operation Mode Using Gas Diffusion Electrodes. *Chem. Eng. Technol.* **2016**, *39*, 2042–2050.

(19)   Sen, S.; Brown, S. M.; Leonard, M. L.; Brushett, F. R. Electroreduction of Carbon Dioxide to Formate at High Current Densities Using Tin and Tin Oxide Gas Diffusion Electrodes. *J. Appl. Electrochem.* **2019**, *49*, 917–928.

(20)   Berengue, O. M.; Rodrigues, A. D.; Dalmaschio, C. J.; Lanfredi, A. J. C.; Leite, E. R.; Chiquito, A. J. Structural Characterization of Indium Oxide Nanostructures: A Raman Analysis. *J. Phys. D. Appl. Phys.* **2010**, *43*.

(21)   Wang, Y.; Alsmeyer, D. C.; McCreery, R. L. Raman Spectroscopy of Carbon Materials: Structural Basis of Observed Spectra. *Chem. Mater.* **1990**, *2*, 557–563.

(22)   Seong, M. J.; Mićić, O. I.; Nozik, A. J.; Mascarenhas, A.; Cheong, H. M. Size-Dependent Raman Study of InP Quantum Dots. *Appl. Phys. Lett.* **2003**, *82*, 185–187.